# SUPPLEMENTARY INFORMATION — Phonon-tunneling dissipation in mechanical resonators

Garrett D. Cole,[1,*] Ignacio Wilson-Rae,[2,†] Katharina Werbach,[1] Michael R. Vanner,[1] and Markus Aspelmeyer[1]

[1] *Vienna Center for Quantum Science and Technology (VCQ), Faculty of Physics, University of Vienna, Boltzmanngasse 5, A-1090 Vienna, Austria.*

[2] *Technische Universität München, 85748 Garching, Germany.*

(Dated: February 14, 2011)

## Supplementary Figures

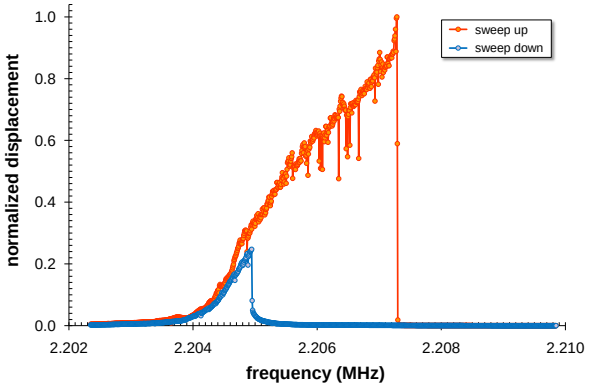


**Supplementary Figure S1. Measured bistable driven response of the antisymmetric mode** – For large drive amplitudes the expected hysteresis is observed. The red points are recorded for an increasing frequency of the drive (sweep up), while the blue dataset is generated with a decreasing frequency (sweep down). The significant nonlinearity present in this mode helps to distinguish it from the free-free resonance.

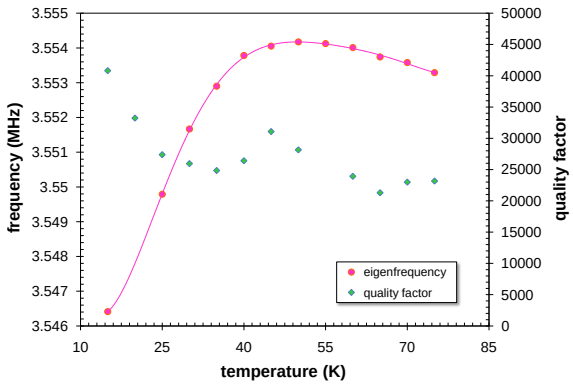


**Supplementary Figure S2. Temperature dependence of the resonant frequency and $Q$-value for the symmetric (free-free) mode** – Measurements were performed on a representative resonator fabricated from the AlGaAs-on-Ge materials system with auxiliary beams near the ideal nodal positions for the fundamental flexural mode of the central plate. The curve shown for the resonant frequency is simply a guide for the eye.

# Supplementary Methods

### A: Numerical verification with bridge geometries

Our generic symmetric inscribed structure includes the particular case of bridge geometries with no undercut for which a simple variant of the method used in Ref. [24] allows us to obtain an analytical approximation for the $Q$-value of the fundamental mode $Q_{c-c}$ valid for $3\pi\mathsf{t}/2L \ll 1$. Our scenario differs from the one considered in Ref. [24] in two ways: (i) there is now a single half-space support instead of two and (ii) its free surface is oriented parallel to the beam's axis instead of perpendicular to it. Thus, for the fundamental flexural mode as the resonant wavelength in the support is much larger than the bridge length $L$, to lowest order in $(\mathsf{t}/L)^2$ the stresses at both clamping points add coherently so that the overall effect of (i) is to double the dissipation. In turn (ii) implies that the roles of the dimensionless displacements for compression and bending are interchanged so that the dissipation of the vertical bending modes are further corrected by a factor of $\tilde{u}_c/\tilde{u}_v$. Thus if we consider that the support and resonator are made of the same material characterized by a Poisson ratio $\nu = 1/3$ we obtain

$$Q_{c-c} = \frac{0.92\, L^5}{\pi^4 \mathsf{w}\mathsf{t}^4}\,. \tag{S1}$$

Hence as a non-trivial check we have applied our numerical method to the fundamental mode of clamped-clamped square beam monolithic geometries with no undercut, $\nu = 1/3$, and aspect ratios $L/\mathsf{t}$ ranging from 15 to 40 and compared the results with those corresponding to Eq. (S1). We find a discrepancy $\epsilon$ that decreases monotonically from 20% to 4% which is consistent with the rough heuristic estimate $\epsilon \sim 3\pi\mathsf{t}/2L$.

### B: Analysis of Completed Devices

The resonator layout we have designed features 16 devices on chip, each with identical central resonator dimensions (nominally $130 \times 40\,\mu\mathrm{m}^2$). The 16 devices are divided into two sub-units featuring different outer radii (116 um and 131 um respectively), which are included in order to probe the effects of the auxiliary beam length on the dissipation. Finally, each of the two subsets contains 8 variations of the auxiliary beam contact position, varying from the center to the extreme outer edge of the central beam, with a single design chosen

to match the theoretically calculated node position (auxiliary beam positions of 13, 21, 29, 37.4, 44, 50, 56, and finally, 62.5 $\mu$m). To ensure a thorough investigation of each geometry, two separate but nominally identical chips are measured.

Central to this study is an accurate determination of the geometric properties of the optomechanical resonators. Thus, we employ a variety of analytical techniques for the characterization of these devices as detailed below. We find that the actual thickness of the DBR is 6.67 $\mu$m, the central resonator dimensions are enlarged by 1 $\mu$m at each free edge as compared with the nominal design values, and finally, $L_{\mathrm{und}}$ is destructively measured post characterization and found to be on average 27 $\mu$m. In turn the microfabrication procedure detailed Ref. [50] entails $h \sim L_{\mathrm{und}}$.

Thickness: In order to accurately determine the physical thickness of the resonators, we rely on measurements of the DBR reflectance spectrum. This procedure begins by recording the reflectance of the mirror stack (on wafer) as a function of wavelength via spectrophotometry. A transmission matrix model is then used to fit the measured high-reflectivity stop-band; the individual layer thicknesses are adjusted assuming constant (fixed percentage) growth errors for the constituent films. Note that the wavelength of peak reflectivity of the mirror is highly sensitive to variations in layer thickness. In fact for this structure, a 1 nm variation in the individual layer thickness shifts the wavelength of peak reflectivity by approximately 10 nm. Relying on accurate knowledge of the room temperature refractive index of the binary films, we realize a minimum wavelength resolution of $\pm$1nm; thus, the thickness accuracy is better than 20 nm for the DBR. From this analysis we have determined that the actual thickness of the DBR is slightly shorter than desired at 6.67$\mu$m with a peak on-wafer reflectance near 1060 nm at room temperature (ideal target thickness of 6.86$\mu$m, corresponding to a peak wavelength of 1078 nm at 300 K). The thickness is further verified by scanning probe measurement of the DBR following the anisotropic etch of the epitaxial layers. The profilometer provides an upper limit to the DBR thickness, as additional etching arising from surface sputtering of the Ge substrate is unavoidable. These measurements yield a conservative thickness estimate between 6.7$\mu$m and 6.8$\mu$m, verifying the more accurate spectrophotometer derived value.

Resonator Dimensions: The lateral dimensions of the resonators are determined by obtaining high resolution micrographs of each individual structure in a field emission scanning electron microscope (Zeiss Gemini). Image analysis shows that the lateral dimensions of the

resonators have expanded by $+1\,\mu$m on each edge, with the following results: reducing the nominal external support diameter by $2 \pm 0.3\,\mu$m, increasing the auxiliary beam width from $5\,\mu$m to $7 \pm 0.3\,\mu$m, and increasing the overall lateral dimensions of the resonator by $2\,\mu$m to $132 \pm 0.3\,\mu$m and $42 \pm 0.3\,\mu$m. Additionally, a combination of process non-idealities (non-optimized exposure or development times) during lithography result in the formation of a 3-$\mu$m-radius fillet of at each corner of the device. These results are fed back into the CAD model of the resonator in order to generate the true resonator geometry for simulation. An overlay of the simulated resonator geometry and micrographs obtained via scanning electron microscopy can be seen in Fig. 3(a). Note that the resonators used in this study were not subject to potentially damaging energetic processes beyond the required plasma etching, including both SEM and FIB (as described below), until all dissipation measurements had been completed.

Undercut: In order to perform measurements of the support undercut distance, a dual beam SEM/FIB (Zeiss Gemini) is utilized to mill a window through the DBR and expose the underlying germanium. Because the GaAs/AlAs heterostructure is opaque to visible light, it is not possible to simply view the undercut distance with an optical microscope. This method allows for an accurate determination of the lateral etch distance below the supports. Image analysis yields an average distance of 27 $\mu$m for the structures. Note that multiple chips of identical geometry were released simultaneously in a single process run, in order to ensure repeatability in the resonator dimensions. Selected measurements across the chip verify that the undercut length is constant for the resonators studied here (measured values fall between 26.5 and 28.2 $\mu$m).

### C: $Q$-value and frequency measurements

We utilize two options for driving and characterizing the resonance of interest: (i) by applying broadband white noise to the piezo disc for extraction of the mechanical frequency spectrum (simultaneously driving all modes within the system bandwidth), and (ii) by exciting a desired mode resonantly with a sinusoidal voltage input, abruptly shutting off the drive, and then recording the free-ringdown of the structure. In the first method, $Q$ is extracted by measuring the width of the resonance of interest, while in the latter, the single-shot amplitude decay time of the ringing structure provides the damping rate of the resonator.

For data analysis, we employ a combination of spectral fitting with a Lorentzian function, with linear-regression-based fitting of a decaying exponential in the case of the ringdown data. The envelope of the raw ringdown signal is created by first squaring the dataset (in order to utilize both the positive and negative components of the decaying sinusoid) and then averaging over a 10-20 period window (it is important to note that a typical ringdown dataset contains more than $1.5 \times 10^3$ periods of oscillation). Finally, to linearize the data, we simply take the natural logarithm of the mean-squared amplitude. In contrast to the single-shot ringdown datasets, the spectral measurements require multiple averages for a clean signal (typically $\sim 50 - 100$). The Lorentzian fit parameters include the amplitude, center frequency, and full width at half maximum (FWHM), with the latter two used for calculating $Q$ from their ratio. The fast Fourier transform (FFT) of the ringdown signal can also be used to determine the eigenfrequency, while the $1/e$ decay time $\tau$ allows for the extraction of the resonator quality factor via the relation $\tau = Q/\pi f$.

Mode identification is realized by comparing the resonator frequency response as a function of geometry with the simulated eigenfrequency values. The modes are further distinguished by the relative geometric-induced nonlinearity at resonance. The desired free-free mode remains linear to the limits of our piezoelectric-based inertial drive. On the other hand, the neighboring anti-symmetric mode exhibits a significant hardening spring Duffing response and can readily be driven into a bistable regime as shown in Supplementary Figure S1. Care is taken to drive this mode below the threshold for bistability to avoid complications in dissipation extraction. This marked difference in the responses of these two types of modes is consistent with their free-free versus clamped-clamped nature[4].

To each dissipation mechanism there is an associated dispersive effect induced by the interactions with the corresponding environment that shifts the resonant frequencies. For a given resonance ($\omega_R$) this shift can be positive or negative depending on whether the environmental spectrum is dominated, respectively, by modes with frequencies lower or higher than $\omega_R$. In turn, the two types of modes have markedly different surface-to-volume ratios, larger for the antisymmetric resonance and smaller for the symmetric one; exhibit a positive shift which is substantially larger for the symmetric mode, and a "background" dissipation that is larger for the antisymmetric one (cf. Fig. 3). These facts can be reconciled by assuming that two materials-related dissipation mechanisms contribute to the "background": a bulk one leading to an overall positive shift which is the same for both types of modes, and a

surface one leading to a smaller negative shift that naturally scales as the surface-to-volume ratio. In turn, theoretical estimates for the phonon-tunneling induced shift yield a negligible *negative* shift that should also follow the mode profile leading to a significant modulation that is not observed. Likewise, mode coupling between the different resonators would also be incompatible with a constant shift.

Currently, the nature of the background dissipation mechanism in these resonators is unknown. It is important to point out that these devices are grown using a heteroepitaxial materials platform: in this implementation the GaAs/AlAs DBR is grown on an off-cut germanium substrate[50]. The advantage of the germanium substrate is that it significantly simplifies processing (enabling the use of a gas-phase release process via $XeF_2$), resulting in an extremely high yield and excellent geometric control — ideal characteristics for our dissipation study. Unfortunately, as discussed in Ref. [50], the materials quality is compromised in this implementation due to the slight lattice mismatch between Ge and GaAs/AlAs. Here misfit dislocations and residual anti-phase boundaries in the bulk of the resonator lead not only to a reduced surface quality (with an RMS roughness value exceeding 30Å), but also an enhanced background dissipation level. In comparison, we have fabricated nominally identical resonators (i.e. utilizing the same lithographic mask) from a homoepitaxial AlGaAs Bragg stack grown on a binary GaAs substrate[51]. The improved surface roughness measured for this structure ($\sim$ 6Å) points towards a significantly reduced defect density; this is also supported by the increased maximum quality factor, $Q$, which is measured to be $> 8 \times 10^4$ at cryogenic temperatures[51].

We have additionally investigated the temperature dependence of the quality factor, albeit over a limited range. As mentioned in the Methods Section, at room temperature thermoelastic (TED) damping limits the achievable $Q$ to $< 10^4$. In Supplementary Figure S2 we include the temperature dependence of $Q$ in the range $20-80\,\mathrm{K}$ for a resonator dominated by the background dissipation given that the auxiliary beams are placed near the nodal positions. By 80 K, the theoretical TED limited $Q$ exceeds $5 \times 10^5$, at this point the device becomes limited by the aforementioned background damping channel. As the temperature decreases, the device exhibits a reduced dissipation with a local maximum in $Q$ near 50 K, potentially corresponding to the zero-crossing of the thermal expansion in GaAs as previously observed in Ref. [52].The large viewport in our cryostat as well as the thermally-insulating piezoelectric disc, limit the minimum realizable temperature to $\sim 15\,\mathrm{K}$. It appears that with

further cooling it would be possible to realize even higher quality factors.

## Supplementary References

[52] Okamoto, Hajime, Ito, Daisuke, Onomitsu, Koji & Yamaguchi, Hiroshi Thermoelastic damping in GaAs microme-chanical resonators. In *Pys. Stat. Sol.* C, 5, 2920-2922 (2008). 34th Int. Symp. on Compound Semiconductors.

---

* garrett.cole@univie.ac.at

† ignacio.wilson-rae@ph.tum.de

G.D.C and I.W.R. contributed equally to this work.